Accepted Manuscript

A top-down approach to build Li_2S@rGO cathode composites for high-loading lithium–sulfur batteries in carbonate-based electrolyte

Maximiliano Zensich, Tony Jaumann, Gustavo M. Morales, Lars Giebeler, César A. Barbero, Juan Balach

PII: S0013-4686(18)32446-0

DOI: https://doi.org/10.1016/j.electacta.2018.10.184

Reference: EA 32983

To appear in: *Electrochimica Acta*

Received Date: 1 August 2018

Revised Date: 22 October 2018

Accepted Date: 30 October 2018

Please cite this article as: M. Zensich, T. Jaumann, G.M. Morales, L. Giebeler, Cé.A. Barbero, J. Balach, A top-down approach to build Li_2S@rGO cathode composites for high-loading lithium–sulfur batteries in carbonate-based electrolyte, *Electrochimica Acta* (2018), doi: https://doi.org/10.1016/j.electacta.2018.10.184.

This is a PDF file of an unedited manuscript that has been accepted for publication. As a service to our customers we are providing this early version of the manuscript. The manuscript will undergo copyediting, typesetting, and review of the resulting proof before it is published in its final form. Please note that during the production process errors may be discovered which could affect the content, and all legal disclaimers that apply to the journal pertain.

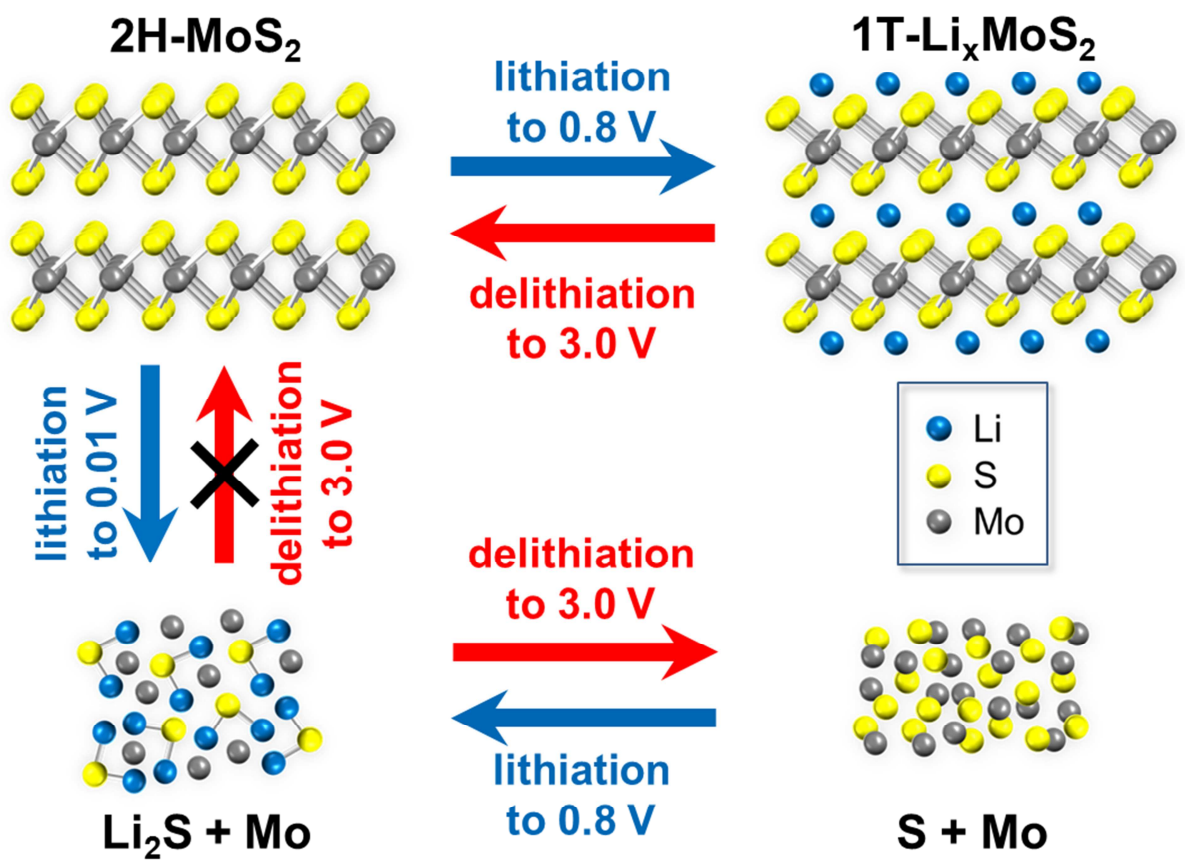
2H-MoS2
1T-LixMoS2
lithiation
to 0.8 V
delithiation
to 3.0 V
lithiation
to 0.01 V
delithiation
to 3.0 V
Li
S
Mo
delithiation
to 3.0 V
lithiation
to 0.8 V
Li2S + Mo
S + Mo

ACCEPTED

ACCEPTED MANUSCRIPT

A top-down approach to build Li_2S@rGO cathode composites for high-loading lithium–sulfur batteries in carbonate-based electrolyte

*Maximiliano Zensich [a], Tony Jaumann [b], Gustavo M. Morales [a], Lars Giebeler [b], César A. Barbero [a], Juan Balach [a,]**

[a] Department of Chemistry, Universidad Nacional de Río Cuarto-CONICET, Route 36 Km 601, X5804ZAB, Río Cuarto, Argentina.

[b] Leibniz Institute for Solid State and Materials Research (IFW) Dresden e.V., Helmholtzstraße 20, 01069 Dresden, Germany.

ACCEPTED MANUSCRIPT

*Corresponding Author: Phone: +54 358 4676 157, e-mail address: jbalach@exa.unrc.edu.ar

ABSTRACT With a notable advantage in terms of specific capacity (1166 mAh g^{-1}), lithium disulfide (Li_2S) has been considered a promising cathode material for high-energy-density lithium–sulfur (Li–S) batteries. In contrast to pure sulfur, Li_2S opens the opportunity to implement alternative anodes such as silicon or graphite instead of hardly controllable lithium metal. However, its intrinsically low conductivity and the formation of soluble lithium polysulfide species during cell operation resulting in a poor cycling stability, especially in carbonate-based electrolytes. Herein, a reduced graphene oxide-wrapped Li_2S particles (Li_2S@rGO) electrode is presented for improving the electrochemical performance of Li–S batteries in carbonate-based electrolytes. A hydrothermally prepared rGO-covered MoS_2 particles composite was fully lithiated and irreversible decomposed at 0.01 V *vs*. Li/Li^+ to *in situ* produce a Li_2S@rGO composite with a high Li_2S loading of ≈5 mg cm^{-2}. Despite operating Li–S cells in a conventional carbonate-based electrolyte, the resulting cathode exhibits high initial capacity (975 mAh g_{Li2S}^{-1} and 1401 mAh g_S^{-1} at 0.1 C), low degradation rate (0.18% per cycle after 200 cycles at 2 C) and excellent Coulombic efficiency (≈99.5%). This work provides a simple strategy to fabricate practical high-loading Li_2S cathodes for high-performance Li–S batteries "free" of polysulfide shuttle phenomenon.

Keywords: MoS_2 electrode, Li_2S cathode, carbonate-based electrolyte, lithium-sulfur battery

1. Introduction

Lithium–sulfur (Li–S) batteries have received significant attention in the last decade because of their overwhelming theoretical energy density of 2.6 kWh kg^{-1}—around one order higher than conventional lithium-ion (Li-ion) batteries consisting of intercalation cathode compounds—at a practically low cost, making them the prime alternative for next-generation energy storage devices capable to satisfy upcoming market energy demands [1-3].

Unfortunately, the practical application of Li–S batteries is still delayed by the low sulfur (re)utilization and the fast capacity fading caused by the poor electrical/ionic conductivity of sulfur/lithium (di)sulfide (Li_2S_2/Li_2S, $\rho_{Li2S} > 10^{12}$ Ωm, $D_{Li} \approx 10^{15}$ cm^2 s^{-1}), the large volume changes of the active material during cycling and, principally, the so-called "shuttle effect" of lithium polysulfide (LiPS) intermediates. This undesired phenomenon involves the dissolution of long-chain polysulfides (Li_2S_n, $8 \geq n > 4$) in commonly used aprotic electrolytes formed during cell discharge which, driven by concentration gradient and electric field forces, tend to migrate from the cathode to the anode. Once the soluble high-order LiPSs reach the metallic lithium anode, they are reduced to insulating Li_2S_2/Li_2S products to further form a passivation film on anode surface. Furthermore, the unreacted LiPS intermediates located in the anode side are re-oxidized during charging and diffuse back to the sulfur cathode. This phenomenon is mainly responsible for active material loss, high self-discharge, low Coulombic efficiency, fast capacity decay and, consequently, poor cycle stability [1, 4-6]. To address the above daunting and challenging issues, extensive work adopting different strategies has already been done including engineering design of novel nanostructured sulfur hosts [3, 7-9], development of specific electrolyte additives capable to interact with polar LiPS intermediates [10, 11], reconfiguration of Li–S cell setup by employing a conductive interlayer or hybrid separator coated with a functional layer [12-15] and protection of lithium anodes [16, 17]. Despite these exciting progresses, satisfying solutions that can manage shuttle effect suppression and

cycling stability requirements at high sulfur loadings is still a challenge for large-scale energy storage systems [18, 19]. Thus, a more versatile strategy is highly required.

To meet on part of this strategy, we turn our attention to the chemistry behind the electrochemical reaction of Li and molybdenum disulfide (MoS_2). The layered transition metal dichalcogenide, MoS_2, has been extensively studied as both intercalation (as cathode) and conversion (as anode) electrodes for primary and secondary lithium batteries, respectively [20, 21]. Previous research works described that MoS_2 (2H-phase) reversibly reacts with one mole of Li^+ ions to form Li_xMoS_2 (1T-phase) *via* an intercalation reaction at a voltage of ≈1.1 V *vs.* Li/Li^+ ($MoS_2 + xLi^+ + xe^- \leftrightarrow Li_xMoS_2$; $0 < x \leq 1$) [22]. At voltages <0.6 *vs.* Li/Li^+, the electrochemical conversion of MoS_2 to Li_2S and metallic Mo occurs for reactions of more than one mole of Li per mole of MoS_2 [23]. Interestingly, a large initial discharging capacity above 1100 mAh g^{-1} is usually observed, which is a significantly high value considering that the theoretical capacity of MoS_2 is 669 mAh g^{-1} for a complete conversion reaction ($MoS_2 + 4Li^+ + 4e^- \rightarrow 2Li_2S + Mo$). This over-capacity is generally attributed to the electrolyte degradation and the storage capacity resulting from the Li^+ intercalation/insertion on defect sites of MoS_2 or into carbon structures used as support/conductive additive [24, 25]. In addition, it is generally believed that the discharging product Li_2S is reversibly converted to MoS_2 in the subsequent charging process. However, experimental and theoretical studies [22, 23, 26-28] have proven that after complete decomposition of MoS_2 to Li_2S (and Mo) the following charging/discharging cycles are governed by the chemistry of the Li_2S/S redox couple ($Mo + 2Li_2S \leftrightarrow Mo + 2S + 4Li$). Therefore, the reaction mechanism of the electrode acts like a sulfur electrode after the initial cycle, which mainly contributes to the specific capacity in the subsequent discharging/charging cycles (Scheme 1).

On the other hand, two-dimensional graphene sheets, graphene oxide (GO) and reduced graphene oxide (rGO) have been widely used in various important applications such as electrochemical energy storage and conversion, catalysis, biomedicine, sensing, transistors

and optoelectrical devices due to their high mechanical strength, high surface area, great optical absorbance, and high thermal and electrical conductivity [29-33]. Furthermore, due to the large aspect ratio of the 2D GO sheets and the large number of functional groups on GO, the self-assembly interactions of GO during reduction and mutual restriction of mobility, e.g. during hydrothermal processes, the GO could result in slightly reduced graphene materials with three-dimensional (3D) architectures [34, 35].

Scheme 1.

In this contribution, a reduced graphene oxide-wrapped Li_2S particles (Li_2S@rGO) composite material was formed by simple electrochemical conversion of MoS_2 particles covered by few-layered rGO and used as a Li_2S cathode for Li–S batteries. The hydrothermally prepared rGO-covered MoS_2 particles composite was completely lithiated at low discharging voltages (i.e. 0.01 V *vs*. Li/Li^+) to *in situ* produce a Li_2S@rGO composite with a high Li_2S loading of ≈5 mg cm^{-2}. The resulting cathode tested in a conventional carbonate-based electrolyte system exhibits high initial capacity (975 mAh g_{Li2S}^{-1} and 1401 mAh g_S^{-1} at 0.1 C), low degradation rate (0.18% per cycle after 200 cycles at 2 C) and notable Coulombic efficiency (≈99.5%). Such excellent electrochemical performance of the Li_2S@rGO cathode is attributed to the unique architecture of the resulting Li_2S@rGO composite which facilitates the fast diffusion of ions/electrons, boosts electrode kinetic, buffers volume changes during cycling and protects the active material from undesirable interactions with electrolytes. This work provides a simple strategy to fabricate practical highly loaded Li_2S cathodes for high-performance Li–S batteries in the absence of the shuttle phenomenon.

2. Experimental section

2.1 Graphene oxide synthesis. Graphene oxide (GO) was synthesized through a modified Marcano's method by oxidation of pure natural graphite powder [36]. Briefly, a mixture of concentrated H_2SO_4 (Cicarelli, 95–98 vol.%) and H_3PO_4 (Cicarelli, 85 vol.%) (9:1 v/v) was added dropwise to a stirred mixture of $KMnO_4$ (Cicarelli) and graphite flakes (Aldrich) (6:1 p/p) at a temperature of 20 °C. The resulting mixture was maintained at 20 °C under stirring for 96 h. Then, the mixture was slowly added to a beaker containing a frozen solution of H_2O_2 (Cicarelli, 30 vol.%) to deactivate the reaction. The final yellow dispersion was first purified by successive decantation of the graphite oxide. After the precipitation, the supernatant was discarded and the precipitated solid was re-suspended in deionized water (1 L). This process was repeated 3–4 times more. Then, the purification was continued by six consecutive centrifugation steps (6000 rpm, 30 min) and finally, the remaining solid was re-suspended in deionized water and dialyzed against deionized water until the conductivity of the dialysate was lower than 5 μS cm^{-1}. The obtained GO dispersion was concentrated to 3.8 mg ml^{-1} and stored in darkness at 5°C.

2.2 rGO and MoS_2@rGO composite preparation. The rGO was obtained by a hydrothermal treatment of a GO aqueous dispersion. First, 20 mL of the concentrated GO dispersion (3.8 mg ml^{-1}) was diluted to a final volume of 38 mL with deionized water (Fig. S1a). Then, the diluted dispersion was transferred into a PTFE autoclave (Parr Instrument Company mod. 4744), and hydrothermally treated at 180 °C for 6 h. The obtained hydrogel was washed several times with deionized water. Finally, the hydrogel was freeze-dried for 48 h to obtain a partially reduced GO aqueous aerogel.

The MoS_2@rGO composite was synthesized following a similar procedure. First, MoS_2 particles (Sigma-Aldrich, 99 wt.%; 187 mg) were dispersed in deionized water (7.5 mL). This dispersion was added dropwise under vigorous stirring to a concentrated GO solution (21 mL, containing approximately 80 mg of GO) followed by the addition of deionized water (11.5 mL) (Fig. S1b). The resulting mixture was stirred for 12 h and further heated at 180 °C for 6 h

in an autoclave (Fig. S1c). The obtained monolithic partially reduced GO-wrapped MoS_2 was washed several times with deionized water and freeze-dried for 48 h (Fig. S1d). Finally, the partially reduced GO and the partially reduced GO-wrapped MoS_2 samples were placed into a horizontal quartz tube and heated at 900 ºC for 30 min under argon flow to obtain the rGO and the MoS_2@rGO composite.

2.3 Characterization. The morphology and structure of the few-layered rGO and the MoS_2@rGO composite materials were analyzed using a Zeiss Leo Gemini 1530 scanning electron microscope (SEM) and a FEI Tecnai F30 transmission electron microscopy (TEM) equipped with a field emission gun (FEG) working at 300 kV. Energy-dispersive X-ray (EDXS) measurements were conducted with a Bruker detector (XFlash 6) attached to the SEM. Nitrogen physisorption experiments and the respectively data analysis were performed using a Quantachrome Quadrasorb SI instrument and a Quantachrome Quadrawin 5.05 software. The samples were degassed under dynamic vacuum at 150 ºC for 24 h prior to measurement. Specific surface area and pore size distribution were calculated using the multi-point Brunauer–Emmett–Teller (BET) and the Quenched Solid Density Functional Theory (QSDFT) methods, respectively. The total pore volume was determined at a relative pressure of 0.97. X-ray power diffraction (XRD) measurements were conducted with a STOE Stadi P diffractometer with a curved Ge(111) crystal monochromator and a 6°-position sensitive detector. Before these measurements, the MoS_2@rGO sample was fixed with collodion glue onto an acetate foil. Diffraction patterns were recorded in the range of $10° \leq 2\theta \leq 80°$ with a step size of $\Delta 2\theta = 0.02°$ in transmission geometry with Cu $K_{\alpha 1}$ radiation. For *post mortem* XRD analysis, the cells containing the MoS_2@rGO electrode were cycled in a voltage range of 0.01–3.0 V *vs*. Li/Li^+ at a current rate of 117 mA g^{-1} and disassembled at a discharging voltage of 0.01 V and a charging voltage of 3.0 V inside an Argon-filled glove box. Afterwards, each electrode was washed three times with dimethyl carbonate and dried under vacuum at room temperature. Finally, the dried samples were pressed between two Kapton

tapes under argon atmosphere to prevent contact with air during the XRD measurement. The MoS_2 content in the MoS_2@rGO composite was determined by thermogravimetric analysis (TGA) after combustion in synthetic air at 700 °C (10 °C min^{-1} heating rate) using a Netzsch Jupiter STA 449C.

2.4 Li_2S@rGO cathode preparation and electrochemical tests. Coin cells (CR2025) were assembled in an Argon-filled glove box (H_2O < 1 ppm, O_2 < 0.1 ppm). Glass fiber membranes (Whatman) were used as separator. Lithium metal foil (Chempur, 250 μm thick, 13 mm diameter) was used as both reference and counter electrode; thus, all electrode voltages are referred to the Li/Li^+ reference electrode. The conventional carbonate-based electrolyte used consisted of 1 M $LiPF_6$ in ethylene carbonate/dimethyl carbonate (EC/DMC; 1:1 v/v, 100 μL) (LP30 Selectilyte, BASF).

For the preparation of the Li_2S@rGO cathode, a slurry of MoS_2@rGO composite (95 wt.%) and polyacrylic acid (5 wt.%, Sigma-Aldrich, M_v ≈450000) was prepared in ethanol under ambient conditions by shaker-milling for 30 min. Then the ethanol-based slurry was drop-coated onto copper foams with a diameter size of 12 mm and dried at 100 ºC for 20 h. The mass loading on each electrode was determined by a micro-balance (Mettler Toledo XSE) and the initial MoS_2@rGO loading accounts to 8.7–10.3 mg cm^{-2}. This value corresponds to a Li_2S loading of around 4.3–5.1 mg cm^{-2} and a Li_2S content of 46.5 wt.%, considering complete decomposition of MoS_2 after lithiation.

A BaSyTec Cell Test System (CTS) was used for galvanostatic discharge/charge cycling in the voltage range of 0.01–3.0 V at 25 °C (half-cell). Cyclic voltammograms (CV) and electrochemical impedance spectroscopy (EIS) measurements were carried out using a VMP3 potentiostat (Bio-logic). EIS measurements were performed in the frequency range of 300 KHz–10 mHz using an AC voltage amplitude of 10 mV at 3.0 V closed to the open-circuit voltage. As preconditioning step before cycling performance tests, the cells were pre-cycled once in the range of 0.01–3.0 V at a current rate of 117 mA g^{-1} to form the active Li_2S

material. The calculation of specific discharge capacities are based on both the mass of Li_2S (1 C = 1166 mA g^{-1}) and the equivalent mass of sulfur (1 C = 1675 mA g^{-1}).

3. Results and discussion

The morphologies of the prepared samples were observed by SEM and TEM at progressive magnifications as shown in Fig. 1. The rGO shown the typical disordered 3D porous network structure obtained from the hydrothermal treated highly concentrated GO aqueous dispersions (Fig. 1a) [37]. The high magnification SEM image (Fig. 1b) illustrates a porous structure with walls consisting of thin layers of stacked rGO sheets. Despite the number of rGO layers which compose the walls cannot be quantified, the piling of one to few layers of rGO is observed by TEM (Fig. 1c). Previous studies realized on composites produced by hydrothermal co-assembly of rGO and MoS_2 have demonstrated that the MoS_2:rGO ratio in the initial mixture is an important variable, determining the morphology and microstructure of the final assembly [38-40]. As shown in Fig. 1d, despite of the low content of GO, the hydrothermal synthesized heterostructure of MoS_2@rGO also form a self-assembled porous structure. Evidently, the presence of a high content of MoS_2 (86.9 wt.%; Fig. S2) in the composite does not prevent the interaction between the graphene nanosheets to produce physical crosslinks that finally yield the porous hydrogel. High-loading levels of MoS_2 without loss of the 3D network after the hydrothermal treatment are possible only if there is a strong interaction between MoS_2 particles and the GO surface [39]. The interaction of the MoS_2 with oxygen functional groups of GO seems to avoid its segregation and restacking. In fact, high resolution images obtained by SEM (Fig. 1e) and TEM (Fig. 1f) reveal a microstructure arranged by MoS_2 nanostructures well distributed through the carbon matrix. The multiple hexagonal spot pattern in the selected area electron diffraction (SAED) corresponding to the HRTEM image in Fig. 1f indicates the crystalline nature of both components, the AB stacking of rGO and MoS_2 nanosheets (space group $P6_3/mmc$ [41]). The element distribution obtained using energy-

dispersive X-ray spectroscopy (EDXS) demonstrates the coexistence of C, Mo and S, verifying the formation of a hybrid structure where the MoS_2 particles are homogeneously distributed on the carbon architecture (Fig. 1g).

Fig. 1.

The physical properties of both pristine rGO and the MoS_2@rGO composite were investigated by nitrogen physisorption experiments (Fig. 2). Fig. 2a shows the nitrogen physisorption isotherm of rGO which exhibit the major nitrogen adsorption at relative pressures $p/p_0 < 0.05$ with a further steady N_2 uptake at higher relative pressures. This curve shape corresponds to a combination of type I and type IV isotherms, implying the presence of micropores and mesopores in the material [42]. Furthermore, desorption branch shows a small H3-type hysteresis loop, characteristic of aggregates of platy particles giving rise to split-like pores [42]. This result suggests that the split-shaped pores were mainly formed through the aggregation of rGO layers stacked on each other and is in good agreement with the morphology observed previously (Fig. 1a). The specific surface area calculated according to the BET method and the total pore volume on basis of the BJH model of rGO are determined to 608 m^2 g^{-1} and 1.41 cm^3 g^{-1}, respectively. Additionally, the pore size distribution calculated by the QSDFT equilibrium model shows two sharp maxima situated at ≈0.95 and ≈2.69 nm and one broad maximum located at ≈24.4 nm (Fig. 2b), indicating the presence of narrow micro- and mesopores as well as an incipient large mesoporosity contributing to pore structure of rGO. Similar to rGO, the MoS_2@rGO composite also exhibits a combined type I and type IV isotherms with a H3-type hysteresis loop. However, the composite shows an important decrease in both specific surface area and pore volume (66 m^2 g^{-1} and 0.22 cm^3 g^{-1}, respectively), probably due to the low amount of lightweight carbon material in the composite (13.1 wt.% of rGO, Fig. S2) and therewith most of the accessible surface is covered and the

pore system is filled with MoS_2. Fig. 2b also reveals a pore size shift in the composite structure from 0.95 nm to 1.65 nm, to finally form large pores between 1.4 and 4.6 nm. Note that the accessible surface area and mesoporosity remaining in the MoS_2@rGO composite could facilitate the Li^+ ion/electron transfer processes and also buffer the occurring volume changes during intercalation/conversion of MoS_2, thus preventing the degradation of the cathode structure.

The electrochemical properties of the MoS_2 electrode at different discharging cutoff voltages were investigated by galvanostatic discharging/charging voltage profiles at a current density of 117 mA g^{-1}. We focused on the comparison of the electrochemical behavior of the composite in a voltage window between 0.8 and 3.0 V without and with a previous discharging cutoff voltage step reaching 0.01 V for preconditioning to form Li_2S. Fig. 3a displays the representative discharging/charging (lithiation/delithiation) voltage curves of the MoS_2@rGO composite between 0.8 and 3.0 V corresponding to the initial and second cycle. The initial discharging process shows a large voltage plateau positioned at 1.13 V which corresponds to the intercalation of Li cations into the MoS_2 structure to further form a Li_xMoS_2 ($0 \leq x \leq 1$) [43]. In the subsequent discharging process a different electrochemical response with multiple short plateaus is observed, indicating a multistep lithiation mechanism. The difference of the electrochemical behavior between the initial and second discharging process are explained by the induced crystal structure transition from the stable hexagonal 2H phase of MoS_2 to the metastable octahedral 1T phase of the distorted Li_xMoS_2 [44]. Additionally, the initial and second cycle charging curves show two main charging plateaus at ≈2.0 V and ≈2.6 V, which again describe multistep reaction process but here for the delithiation route [45]. Fig. 3b represents the first and second discharging/charging cycle profiles of the MoS_2@rGO composite performed between 0.01 and 3.0 V and between 0.8 and 3.0 V, respectively. For a completed lithiation process to a discharging cutoff voltage of 0.01 V, the first discharging curve exhibits two main reductions plateaus located at ≈1.1 and

≈0.6 V. As discussed above, the discharging plateau at higher voltage is associated to the intercalation/structure transformation of the MoS_2, while the large discharging plateau at lower voltage is attributed to the conversion reaction of Li_xMoS_2 to Li_2S and metallic Mo [27, 28, 43]. Below 0.8 V the organic parts of electrolyte start to decompose, resulting in the formation of the well-known solid electrolyte interphase (SEI) layer. This stable polymeric gel-like SEI matrix, permeable to Li^+ ions, further serves as a crucial protecting layer against the loss of sulfur active material [27, 28]. The succeeding second discharging curve, now with a discharging cutoff voltage of 0.8 V, displays two discharging plateaus at ≈2.0 and ≈1.2 V. This second discharging voltage profile (Fig. S3) is significantly different to that one shown in Fig. 3a, indicating a differing lithiation/reduction mechanism. The shift of the discharging plateau to a higher voltage of ≈2.0 V corresponds to the conversion of sulfur to Li_2S and the lower plateau at ≈1.2 V is apparently associated with the Li adsorption on metallic Mo surface [23, 38, 46], but this latter interpretation is still controversially discussed in literature. A similar study using a cyclic voltammetry technique also demonstrates the formation of Li_2S at a low discharging voltage of ≤ 0.6 V as shown in Fig. S4. During the initial and second charging processes, a dominant voltage plateau at ≈2.2 V is identified, which is related to the oxidation reaction of Li_2S to amorphous sulfur [47, 48]. Additionally, metallic Mo is uninvolved in the following charging/discharging reactions after it is formed but may affect the conductivity of the electrode composite [28].

Fig. 3.

To further support the electrochemical response to the structural changes of the MoS_2 under the lithiation/delithiation process, *ex situ* XRD investigations were performed at a depth of discharge of 0.01 V and a state of charge of 3.0 V (Fig. 4). The fresh MoS_2@rGO cathode shows the distinctive reflections of the MoS_2 corresponding to a hexagonal structure type

(space group $P6_3/mmc$). After the cathode is discharged to 0.01 V, the characteristic reflections of MoS_2 fully disappear to result in the appearance of the typical reflection patterns of Li_2S at 26.9º, 31.0º, 44.6º, 52.9º and 72.2º. Also, a broad reflection situated around 40º is observed, which is characteristic for metallic Mo [49]. When charging the cathode to 3.0 V, no diffraction feature associated to MoS_2 is detected. Instead, the broad reflection at 40º still remains and no further reflections are observed, indicating an amorphous nature of the charging products, most probably small clusters of metallic Mo and amorphous sulfur [23, 27, 28]. Even monoclinic β-S_8, which can be re-formed during charging [50, 51], does not arrange in a long-range ordered state. These results clearly demonstrate that an active Li_2S@rGO composite is formed after complete conversion of MoS_2 covered by rGO and that the reaction mechanism of the electrode behaves like a sulfur electrode in following cycles. It is worth mentioning that lithium intercalation into and de-intercalation out of the few-layered rGO occurs mainly in a range of 0.01 to 0.3 V (Fig. S4b). However, the rGO is not electrochemically affected upon cycling (Fig. S4d).

Fig. 4.

MoS_2-nanostructured carbon composites used as anode material for Li-ion batteries demonstrated good cycling performance during initial 50 cycles when they are tested in a voltage range of 0.01–3.0 V. However, most of the MoS_2-based electrodes contain low MoS_2 contents (< 70 wt.%) and/or low MoS_2 loadings (< 2.0 mg cm^{-1}) which is detrimental for practical applications (see Table S1), since a high carbon content lessens the specific energy density of the electrode. Besides this, a lower active material loading gain better performance of the electrode. In fact, our MoS_2@rGO composite electrode allows a high MoS_2 loading of ≈8.3 mg cm^{-1} cycled between 0.01 and 3.0 V and showed a high initial capacity but a poor capacity retention which is in accordance with previous works (Fig. S5) [22, 27, 28]. The fast

capacity fading is explained by the prompt electrolyte depletion under overdischarging voltages, which increases the cell resistance [27]. This negative effect is easily controlled by limiting the voltage window between 0.8 and 3.0 V in order to stabilize the electrode reactions [22, 27]. Considering the aforementioned features, first we electrochemically form the Li_2S@rGO composite through a complete conversion of the MoS_2@rGO composite after one discharging/charging cycle between 0.01 and 3.0 V (henceforth denoted as activation cycle) and then the electrochemical performance of the Li_2S@rGO composite within a voltage range of 0.8–3.0 V was studied (Fig. 5). As a control cell, a cathode prepared from a mixture of MoS_2 particles and rGO (denoted MoS_2/rGO mixture) with similar MoS_2 content/loading was used. Fig. 5a shows that both Li_2S@rGO composite and Li_2S/rGO mixture cathodes deliver similar high initial capacities of 975 mAh g_{Li2S}^{-1} (1401 mAh g_S^{-1}) and 956 mAh g_{Li2S}^{-1} (1373 mAh g_S^{-1}), respectively. After 50 cycles, the Li_2S@rGO composite cathode exhibits a capacity of 606 mAh g_{Li2S}^{-1} (870 mAh g_S^{-1}) and a notable Coulombic efficiency (CE) of 99.8%. In contrast, the Li_2S/rGO mixture cathode is able to maintain its capacity during the first 20 cycles, but after the 30th cycle the capacity tends to decay faster than for the Li_2S@rGO composite reaching a specific capacity of 448 mAh g_{Li2S}^{-1} (644 mAh g_S^{-1}). In addition, the Li_2S/rGO cathode reveals a CE of 104.5%, which is a good indication for side reactions, *i.e.* decoupling of formed Li_2S particles from the rGO matrix and/or electrolyte depletion. The Li_2S@rGO composite also showed improved rate performance. When gradually increasing the current rate from 0.05 to 2 C, the capacity at each rate remained stable, keeping a reversible capacity of 402 mAh g_{Li2S}^{-1} (577 mAh g_S^{-1}) at 2 C (Fig. 5b). On the other hand, the Li_2S/rGO mixture barely reaches a capacity of 230 mAh g_{Li2S}^{-1} (330 mAh g_S^{-1}) at 2 C, highlighting its inability to retain a proper capacity at high current rates due to slow kinetic processes. In general, the insulating nature of sulfur and Li_2S limits the electron transport in the cathode composite and leads to low active material utilization. Thus, cathodes with high Li_2S content and high Li_2S loading are detrimental for full active material

utilization. It seems that this behavior is stressed at high current rates since not all of the active material is converted during cycling after the current density returned from 2C to 0.1C (cycle 61 of Fig. 5b). However, the Li_2S@rGO composite shows a higher reversibility in capacity at these operation conditions compared with the MoS_2/rGO mixture, indicating superior electrical and ionic pathways in the composite. Nonetheless, both cathodes show good capacity recovery when the current rate returns from 2 to 0.1 C. In an extended cycling test at 2 C, the Li_2S@rGO composite exhibits an initial capacity of 539 mAh g_{Li2S}^{-1} (774 mAh g_S^{-1}), a low degradation rate of 0.18% per cycle (from 2nd cycle) and a remarkable CE of 99.8% after 200 cycles, while the cycling performance of the Li_2S/rGO mixture again lacks in retaining a good reversible capacity at relative high current rate during long cycling tests (Fig. 5c). One reason is found in the formation of LiPS anions in solution which are highly reactive with carbonate solvents and lead to a sudden cell failure [52, 53]. However, the good reversibility of Li_2S@rGO composite cathode in a carbonate-based electrolyte—as the most commonly used electrolyte in Li-ion batteries—reveals the lack of "free" LiPSs in the solution and thus the absence of the "shuttle" phenomenon. The confinement of LiPS intermediates in the composite framework could be explained by the anchoring of LiPS species onto Mo particles *via* Lewis acid-base interactions [26, 54, 55], which are simultaneously embedded into a protecting gel-like polymeric matrix resulting from electrochemically driven electrolyte degradation during activation cycle [26, 27]. To better understand why the Li_2S@rGO composite exhibits superior electrochemical performance compared to the Li_2S/rGO mixture electrode, EIS measurements were performed after the first and 50th cycle at 2 C. As shown in Fig. 5d, the impedance spectra of the cycled cells are composed of two partially overlapping semicircles in the high-to-medium frequency region and a straight slopping line in the low frequency region. The diameter of the semicircles at high-to-medium frequencies is associated to the resistance of the SEI formed on the electrode surface. The charge transfer resistances of the cathodes for the first and the 50th cycle are

52% and 85% smaller for the Li_2S@rGO composite than that of the Li_2S/rGO mixture, indicating faster charge transfer kinetics and better conservation of the SEI film for the composite. This prompt charge transfer capability improves the rate performance of the Li_2S@rGO cathode composite. These results also highlight the benefits of the synergetic effect between the MoS_2 particles and the rGO substrate in the MoS_2@rGO composite to obtain a stable and highly loaded cathode. Compared with recently reported MoS_2/carbon- and Li_2S/carbon-based electrodes, our simple cathode composite demonstrates an excellent electrochemical performance despite of using an electrode with initial high MoS_2 content (82.5 wt.%) and ultrahigh MoS_2 loading (8.29 mg cm^{-2}) even in the presence of a carbonate-based electrolyte which is normally an impassable path for sulfur-based batteries (Table S1).

On the basis of the above-described results, the superior cycling performance of the Li_2S@rGO composite cathode is owed to the synergistic effect between the formed Li_2S particles and the few-layered rGO. The resulting composite with a 3D porous architecture and excellent electrical conductivity facilitates the diffusion of ions/electrons through the electrode network and boosts electrode kinetics, enabling excellent rate capability and enhanced cycling stability.

Fig. 5.

4. Conclusions

Throughout this work, we have proposed a rational and simple strategy to prepare Li_2S@rGO cathodes with high active material loadings for Li–S batteries fully operable in carbonate-based electrolytes due to the absence of the “shuttle effect”, atypical for sulfur batteries. This strategy relies in the complete lithiation and irreversible electrochemical decomposition of MoS_2 particles covered by few-layered rGO *in situ* to form both metallic Mo and Li_2S nanoparticles embedded into a 3D porous rGO/polymeric gel-like SEI matrix. Remarkable,

the resulting Li_2S seems to be in intimate contact with the rGO network due to the lack of soluble LiPS intermediates, allowing the operation of Li–S cells in a conventional carbonate-based electrolyte. By limiting the voltage windows between 0.8 and 3.0 V to avoid side reactions, the Li_2S@rGO cathode containing Li_2S loadings of ≈5 mg cm^{-2} can provide a high reversible capacity, excellent cycling stability and good rate capability. Given its notable capacity advantage over traditional Li_2S/carbon composite cathodes, our MoS_2-derived Li_2S@rGO cathode appeals for high energy density Li–S batteries, and further indicates a simple yet inspiring method for developing high-performance Li_2S-, Na_2S-, Li_2Se-based electrodes for energy storage device applications.

Acknowledgment

The authors thank A. Voß, A. Voidel, R. Buckan and C. Geringswald for their valuable technical support. Dr. R. Hauser from the Fraunhofer IFAM is gratefully acknowledged for providing the copper foam. We also thank A. Ó Braoin for BET measurements. We acknowledge the German Federal Ministry of Education and Research (BMBF) through the Excellent Battery – WING center ‘‘Batteries –Mobility in Saxony’’ (grant no. 03X4637C) for partially funding this work. Additional funding is gratefully provided by the European Union and the Free State of Saxony *via* the NaSBattSy project (SAB grant no. 100234960) and Agencia Nacional de Promoción Científica y Tecnológica (FONCYT-PICT no. 2014-0831).

References

[1] A. Rosenman, E. Markevich, G. Salitra, D. Aurbach, A. Garsuch, F.F. Chesneau, Review on Li-Sulfur battery systems: an Integral Perspective, Adv. Energy Mater., 5 (2015) 1614–6840.

[2] Z.W. Seh, Y. Sun, Q. Zhang, Y. Cui, Designing high-energy lithium-sulfur batteries, Chem. Soc. Rev., 45 (2016) 5605–5634.

[3] H.J. Peng, J.Q. Huang, X.B. Cheng, Q. Zhang, Review on high-loading and high-energy lithium–sulfur batteries, Adv. Energy Mater., 7 (2017) 1700260.

[4] C. Barchasz, F. Molton, C. Duboc, J.-C. Leprêtre, S. Patoux, F. Alloin, Lithium/sulfur cell discharge mechanism: an original approach for intermediate species identification, Anal. Chem., 84 (2012) 3973−3980.

[5] A. Manthiram, Y. Fu, S.-H. Chung, C. Zu, Y.-S. Su, Rechargeable lithium–sulfur batteries, Chem. Rev., 114 (2014) 11751–11787.

[6] Y. Yang, G. Zheng, Y. Cui, Nanostructured sulfur cathodes, Chem. Soc. Rev., 42 (2013) 3018−3032.

[7] X. Ji, K.T. Lee, L.F. Nazar, A highly ordered nanostructured carbon-sulphur cathode for lithium-sulphur batteries, Nat. Mater., 8 (2009) 500–506.

[8] N. Jayaprakash, J. Shen, S.S. Moganty, A. Corona, L.A. Archer, Porous hollow carbon@sulfur composites for high-power lithium–sulfur batteries, Angew. Chem. Int. Ed., 50 (2011) 5904–5908.

[9] J. Balach, J. Linnemann, T. Jaumann, L. Giebeler, Metal-derived nanostructured materials for advanced lithium–sulfur batteries, J. Mater. Chem. A, (2018). DOI: 10.1039/C8TA07220E.

[10] L. Suo, Y.-S. Hu, H. Li, M. Armand, L. Chen, A new class of solvent-in-salt electrolyte for high-energy rechargeable metallic lithium batteries, Nat. Commun., 4 (2013) 1481.

[11] L. Ma, H. Zhuang, Y. Lu, S.S. Moganty, R.G. Hennig, L.A. Archer, Tethered molecular sorbents: enabling metal-sulfur battery cathodes, Adv. Energy Mater., 4 (2014) 1400390.

[12] Y.-S. Su, A. Manthiram, Lithium–sulphur batteries with a microporous carbon paper as a bifunctional interlayer, Nat. Commun., 3 (2012) 1166.

[13] J. Balach, T. Jaumann, M. Klose, S. Oswald, J. Eckert, L. Giebeler, Mesoporous carbon interlayers with tailored pore volume as polysulfide reservoir for high-energy lithium–sulfur batteries, J. Phys. Chem. C, 119 (2015) 4580–4587.

[14] S.-H. Chung, A. Manthiram, Bifunctional separator with a light-weight carbon-coating for dynamically and statically stable lithium-sulfur batteries, Adv. Funct. Mater., 24 (2014) 5299–5306.

[15] J. Balach, H.K. Singh, S. Gomoll, T. Jaumann, M. Klose, S. Oswald, M. Richter, J. Eckert, L. Giebeler, Synergistically enhanced polysulfide chemisorption using a flexible hybrid separator with N and S dual-doped mesoporous carbon coating for advanced lithium–sulfur batteries, ACS Appl. Mater. Interfaces, 8 (2016) 14586−14595.

[16] X. Liang, Z. Wen, Y. Liu, M. Wu, J. Jin, H. Zhang, X. Wu, Improved cycling performances of lithium sulfur batteries with $LiNO_3$-modified electrolyte, J. Power Sources, 196 (2011) 9839–9843.

[17] Q. Pang, X. Liang, A. Shyamsunder, L.F. Nazar, An in vivo formed solid electrolyte surface layer enables stable plating of Li metal, Joule, 1 (2017) 871–886.

[18] S.-K. Lee, Y.J. Lee, Y.-K. Sun, Nanostructured lithium sulfide materials for lithium-sulfur batteries, J. Power Sources, 323 (2016) 174−188.

[19] S.-H. Chung, P. Han, C.-H. Chang, A. Manthiram, A shell-shaped carbon architecture with high-loading capability for lithium sulfide cathodes, Adv. Energy Mater., 7 (2017) 1700537.

[20] C.M. Julien, Lithium intercalated compounds: Charge transfer and related properties, Mater. Sci. Eng. R, 40 (2003) 47–102.

[21] M.-R. Gao, Y.-F. Xu, J. Jiang, S.-H. Yu, Nanostructured metal chalcogenides: synthesis, modification, and applications in energy conversion and storage devices, Chem. Soc. Rev., 42 (2013) 2986−3017.

[22] X. Fang, C. Hua, X. Guo, Y. Hu, Z. Wang, X. Gao, F. Wu, J. Wang, L. Chen, Lithium storage in commercial MoS_2 in different potential ranges, Electrochim. Acta, 81 (2012) 155−160.

[23] J. Xiao, X. Wang, X.-Q. Yang, S. Xun, G. Liu, P.K. Koech, J. Liu, J.P. Lemmon, Electrochemically induced high capacity displacement reaction of PEO/MoS_2/graphene nanocomposites with lithium, Adv. Funct. Mater., 21 (2011) 2840−2846.

[24] Y. Mao, H. Duan, B. Xu, L. Zhang, Y. Hu, C. Zhao, Z. Wang, L. Chen, Y. Yang, Lithium storage in nitrogen-rich mesoporous carbon materials, Energy Environ. Sci., 5 (2012) 7950−7955.

[25] T. Stephenson, Z. Li, B. Olsen, D. Mitlin, Lithium ion battery applications of molybdenum disulfide (MoS_2) nanocomposites, Energy Environ. Sci., 7 (2014) 209−231.

[26] U.K. Sen, P. Johari, S. Basu, C. Nayak, S. Mitra, An experimental and computational study to understand the lithium storage mechanism in molybdenum disulfide, Nanoscale, 6 (2014) 10243−10254.

[27] J. Balach, T. Jaumann, L. Giebeler, Nanosized Li_2S-based cathodes derived from MoS_2 for high-energy density Li–S cells and Si–Li_2S full cells in carbonate-based electrolyte, Energy Storage Mater., 8 (2017) 209–216.

[28] L. Zhang, D. Sun, J. Kang, J. Feng, H.A. Bechtel, L.-W. Wang, E.J. Cairns, J. Guo, Electrochemical reaction mechanism of the MoS_2 electrode in a lithium-ion cell revealed by in situ and operando X-ray absorption spectroscopy, Nano Lett., 18 (2018) 1466–1475.

[29] Y. Zhu, S. Murali, W. Cai, X. Li, J.W. Suk, J.R. Potts, R.S. Ruoff, Graphene and graphene oxide: synthesis, properties, and applications, Adv. Mater., 22 (2010) 3906−3924.

[30] A. M. Dimiev, S. Eigler, Graphene Oxide: Fundamentals and Applications, John Wiley & Sons, United Kingdom, 2016.

[31] H. Huang, J. Zhang, L. Jiang, Z. Zang, Preparation of cubic Cu_2O nanoparticles wrapped by reduced graphene oxide for the efficient removal of rhodamine B, J. Alloys Compd., 718 (2017) 112–115.

[32] X. Liu, T. Xu, Y. Li, Z. Zang, X. Peng, H. Wei, W. Zha, F. Wang, Enhanced X-ray photon response in solution-synthesized $CsPbBr_3$ nanoparticles wrapped by reduced graphene oxide, Sol. Energy Mater Sol. Cells, 187 (2018) 249−254.

[33] J. Wei, Z. Zang, Y. Zhang, M. Wang, J. Du, X. Tang, Enhanced performance of light-controlled conductive switching in hybrid cuprous oxide/reduced graphene oxide (Cu_2O/rGO) nanocomposites, Opt. Lett., 42 (2017) 911–914.

[34] W. Zhou, K. Zhou, D. Hou, X. Liu, G. Li, Y. Sang, H. Liu, L. Li, S. Chen, Three-dimensional hierarchical frameworks based on MoS_2 nanosheets self-assembled on graphene oxide for efficient electrocatalytic hydrogen evolution, ACS Appl. Mater. Interfaces, 6 (2014) 21534−21540.

[35] J. Li, W. Qin, J. Xie, R. Lin, Z. Wang, L. Pan, W. Mai, Rational design of MoS_2-reduced graphene oxide sponges as free-standing anodes for sodium-ion batteries, Chem. Eng. J., 332 (2018) 260−266.

[36] D.C. Marcano, D.V. Kosynkin, J.M. Berlin, A. Sinitskii, Z. Sun, A. Slesarev, L.B. Alemany, W. Lu, J.M. Tour, Improved synthesis of graphene oxide, ACS Nano, 4 (2010) 4806−4814.

[37] Y. Xu, K. Sheng, C. Li, G. Shi, Self-assembled graphene hydrogel via a one-step hydrothermal process, ACS Nano, 4 (2010) 4324–4330.

[38] Y. Gong, S. Yang, L. Zhan, L. Ma, R. Vajtai, P.M. Ajayan, A bottom-up approach to build 3D architectures from nanosheets for superior lithium storage, Adv. Funct. Mater., 24 (2014) 125−130.

[39] L. Jiang, B. Lin, X. Li, X. Song, H. Xia, L. Li, H. Zeng, Monolayer MoS_2–graphene hybrid aerogels with controllable porosity for lithium-ion batteries with high reversible capacity, ACS Appl. Mater. Interfaces, 8 (2016) 2680–2687.

ACCEPTED MANUSCRIPT

[40] X. Xu, L. Wu, Y. Sun, T. Wang, X. Chen, Y. Wang, W. Zhong, Y. Du, High-rate, flexible all-solid-state super-capacitor based on porous aerogel hybrids of MoS_2/reduced graphene oxide, J. Electroanal. Chem., 811 (2018) 96–104.

[41] R.G. Dickinson, L. Pauling, The crystal structure of molybdenite, J. Am. Chem. Soc., 45 (1923) 1466−1471.

[42] K.S.W. Sing, Reporting physisorption data for gas/solid systems with special reference to the determination of surface area and porosity, Pure Appl. Chem., 54 (1982) 2201−2218.

[43] D. Kong, H. He, Q. Song, B. Wang, W. Lv, Q.-H. Yang, L. Zhi, Rational design of MoS_2@graphene nanocables: towards high performance electrode materials for lithium ion batteries, Energy Environ. Sci., 7 (2014) 3320−3325.

[44] T. Wang, S. Chen, H. Pang, H. Xue, Y. Yu, MoS_2-based nanocomposites for electrochemical energy storage, Adv. Sci., 4 (2017) 1600289.

[45] H.D. Yoo, Y. Li, Y. Liang, Y. Lan, Wang, Feng, Y. Yao, Intercalation pseudocapacitance of exfoliated molybdenum disulfide for ultrafast energy storage, ChemNanoMat, 2 (2016) 688−691.

[46] D. Xie, W. Tang, X. Xia, D. Wang, D. Zhou, F. Shi, X. Wang, C. Gu, J. Tu, Integrated 3D porous C-MoS_2/nitrogen-doped graphene electrode for high capacity and prolonged stability lithium storage, J. Power Sources, 296 (2015) 392−399.

[47] J. Balach, T. Jaumann, M. Klose, S. Oswald, J. Eckert, L. Giebeler, Functional mesoporous carbon-coated separator for long-life, high-energy lithium-sulfur batteries, Adv. Funct. Mater., 25 (2015) 5285–5291.

[48] J. Moo, A. Omar, T. Jaumann, S. Oswald, J. Balach, S. Maletti, L. Giebeler, One-pot synthesis of graphene-sulfur composites for Li-S batteries: influence of sulfur precursors, C - J. Carbon Res., 4 (2018) 2.

[49] S.K. Das, R. Mallavajula, N. Jayaprakash, L.A. Archer, Self-assembled MoS_2–carbon nanostructures: influence of nanostructuring and carbon on lithium battery performance, J. Mater. Chem., 22 (2012) 12988−12992.

[50] A. Krause, S. Dörfler, M. Piwko, F.M. Wisser, T. Jaumann, E. Ahrens, L. Giebeler, H. Althues, S. Schädlich, J. Grothe, A. Jeffery, M. Grube, J. Brückner, J. Martin, J. Eckert, S. Kaskel, T. Mikolajick, W.M. Weber, High area capacity lithium-sulfur full-cell battery with prelitiathed silicon nanowire-carbon anodes for long cycling stability, Sci. Rep., 6 (2016) 27982.

[51] N.A. Cañas, S. Wolf, N. Wagner, K.A. Friedrich, *In-situ* X-ray diffraction studies of lithium–sulfur batteries, J. Power Sources, 226 (2013) 313−319.

[52] T. Yim, M.-S. Park, J.-S. Yu, K.J. Kim, K.Y. Im, J.-H. Kim, G. Jeong, Y.N. Jo, S.-G. Woo, K.S. Kang, Effect of chemical reactivity of polysulfide toward carbonate-based electrolyte on the electrochemical performance of Li–S batteries, Electrochim. Acta, 107 (2013) 454–460.

[53] S.S. Zhang, Liquid electrolyte lithium/sulfur battery: Fundamental chemistry, problems, and solutions, J. Power Sources, 231 (2013) 153–162.

[54] C. George, A.J. Morris, M.H. Modarres, M. De Volder, Structural evolution of electrochemically lithiated MoS_2 nanosheets and the role of carbon additive in Li-ion batteries, Chem. Mater., 28 (2016) 7304−7310.

[55] X. Liang, Y. Rangom, C.Y. Kwok, Q. Pang, L.F. Nazar, Interwoven MXene nanosheet/carbon-nanotube composites as Li-S cathode hosts, Adv. Mater., 29 (2017) 1603040.

Caption for Scheme and Figures

Scheme 1. Simplified illustration of the electrochemical reaction mechanism of MoS_2 under different states of discharge (lithiation)/charge (delithiation).

Fig. 1. (a) Low and (b) high magnification SEM and, (c) TEM images of the rGO. (d) Low and (e) high magnification SEM and, (f) TEM with the corresponding SAED patterns (inset) images of the MoS_2@rGO. (g) SEM second electron image and the corresponding EDXS elemental mapping on the scanned area for C, Mo and S; scale bar lengths represent 1 μm. All images shown for rGO and MoS_2@rGO are acquired after a pretreatment heating at 900 ºC for 30 min. under argon atmosphere.

Fig. 2. (a) Nitrogen sorption isotherms and (b) the corresponding pore size distributions of pristine rGO and the MoS_2@rGO composite.

Fig. 3. Galvanostatic discharging/charging voltage profile recorded at a current rate of 177 mA g^{-1} within a potential range of (a) 0.8 V ≤ U ≤ 3.0 V and (b) 0.01 V ≤ U ≤ 3.0 V and 0.8 V ≤ U ≤ 3.0 V for the first and second cycle, respectively.

Fig. 4. *Ex situ* XRD patterns of the fresh MoS_2@rGO cathode, the cathode discharged to 0.01 V and the cathode charged to 3.0 V. The Kapton tape pattern and the Bragg positions of MoS_2 ($P6_3/mmc$), Li_2S (Fm-3m) and Mo (Im-3m) are used as references.

ACCEPTED MANUSCRIPT

Fig. 5. (a) Cycling performance at a current rate of 0.1 C, (b) rate performance, (c) long-term cycling performance at a current rate of 2 C and (d) Nyquist plots of the first and 50th cycle for the half-cells with Li_2S@rGO composite and Li_2S/rGO mixture cathodes cycled at 2 C. All the cells were tested between 0.8 and 3.0 V after activation.

ACCEPTED MANUSCRIPT

Scheme and Figures

Scheme 1

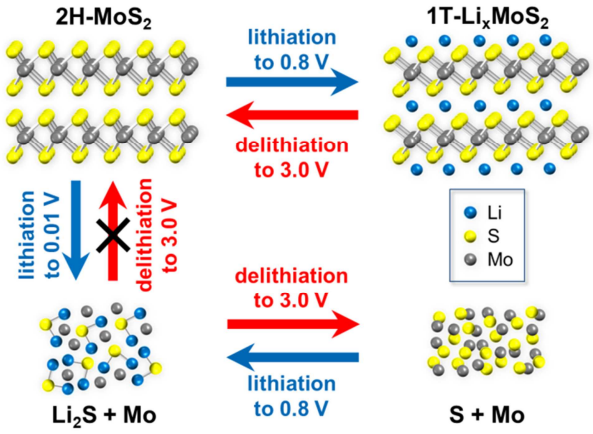

Fig. 1

ACCEPTED MANUSCRIPT

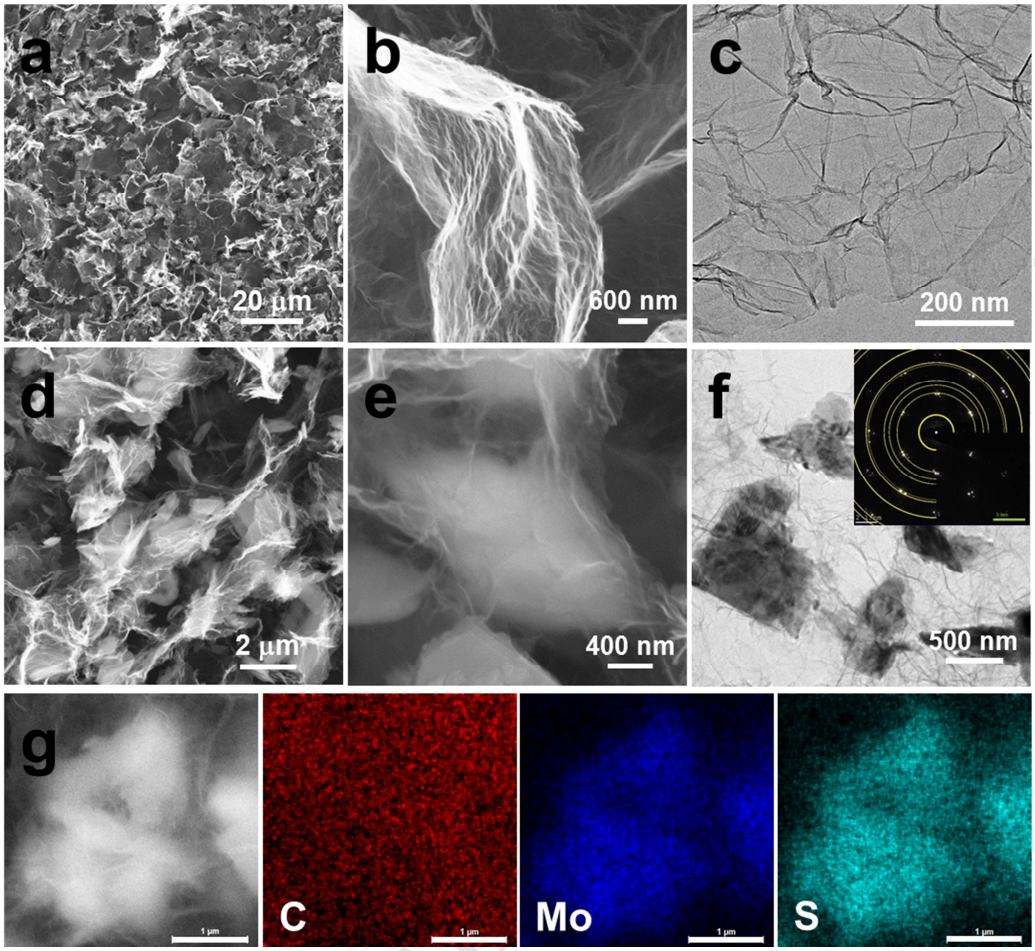
a
20 μm
b
600 nm
c
200 nm
d
2 μm
e
400 nm
f
500 nm
g
C
Mo
S

Fig. 2

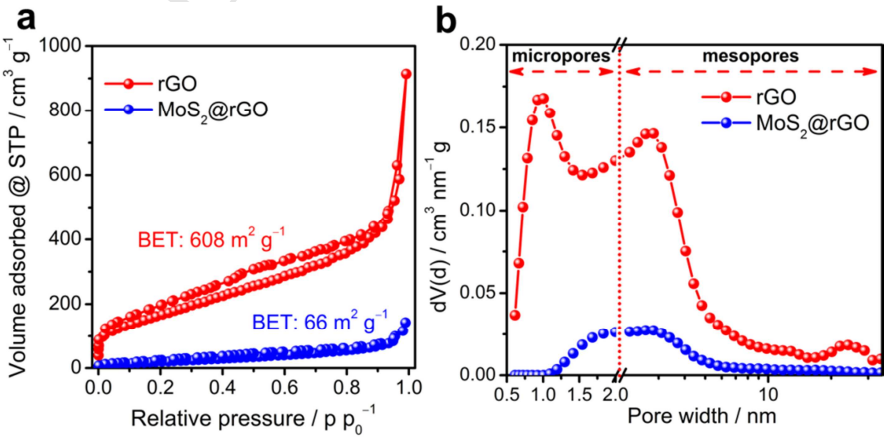
a
Volume adsorbed @ STP / cm3 g-1
rGO
MoS2@rGO
BET: 608 m2 g-1
BET: 66 m2 g-1
Relative pressure / p p0-1
b
micropores
mesopores
rGO
MoS2@rGO
dV(d) / cm3 nm-1 g
Pore width / nm

Fig. 3

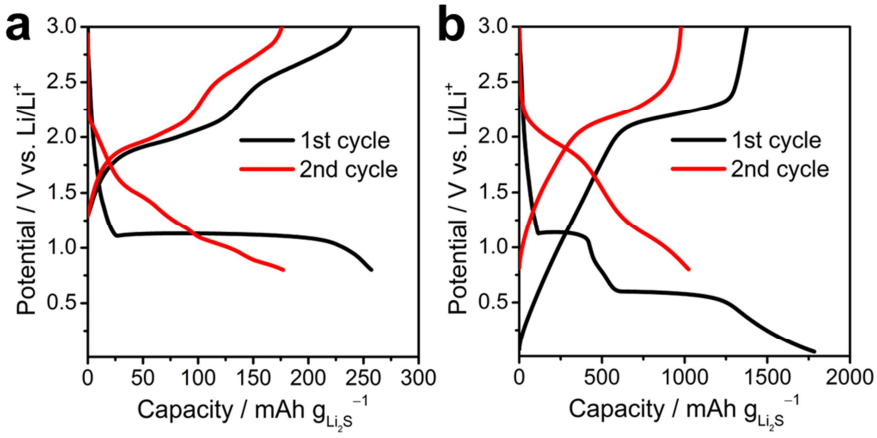
a
b
Potential / V vs. Li/Li+
Capacity / mAh g$_{Li_2S}^{-1}$
1st cycle
2nd cycle

Fig. 4

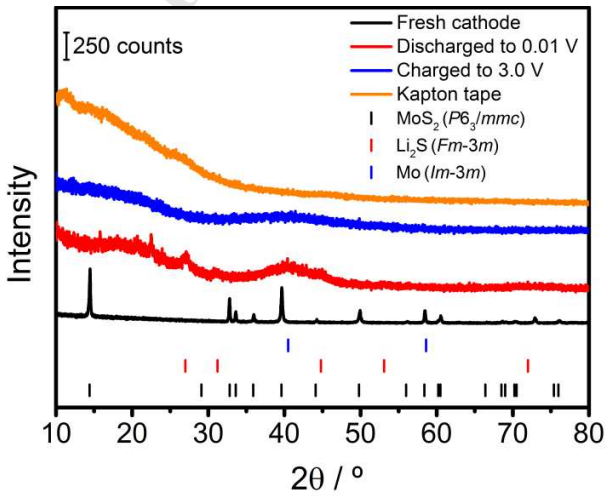
250 counts
Fresh cathode
Discharged to 0.01 V
Charged to 3.0 V
Kapton tape
MoS$_2$ (P6$_3$/mmc)
Li$_2$S (Fm-3m)
Mo (Im-3m)
Intensity
2θ / °

Fig. 5

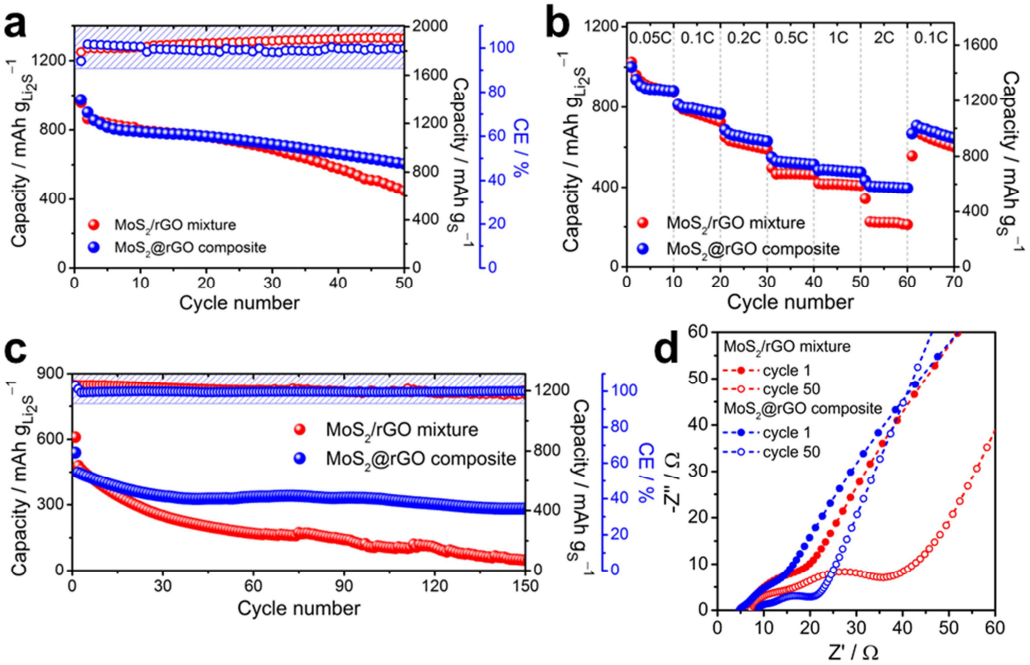

ACCEPTED MANUSCRIPT